Elys deficiency constrains Kras-driven tumour burden by amplifying oncogenic stress

Kimberly J Morgan[1,2], Karen Doggett[1,2], Fan-Suo Geng[1,3], Lachlan Whitehead[2,4], Kelly A Smith[5,6], Benjamin M Hogan[6,7], Cas Simons[6,8], Gregory J Baillie[6], Ramyar Molania[2,9], Anthony T Papenfuss[2,9], Thomas E Hall[6], Elke A Ober[10], Didier Y R Stainier[11], Zhiyuan Gong[12] and Joan K Heath[1,2,*]

[1]Epigenetics and Development Division, Walter and Eliza Hall Institute of Medical Research, Parkville, Victoria 3052, Australia

[2]Department of Medical Biology, University of Melbourne, Parkville, Victoria 3010, Australia

[3]Genomics and Epigenetics Division, Garvan Institute of Medical Research, Darlinghurst, New South Wales, Australia and St Vincent's Clinical School, Faculty of Medicine, University of New South Wales, New South Wales 2010, Australia

[4]Centre for Dynamic Imaging, Advanced Technology and Biology Division, Walter and Eliza Hall Institute of Medical Research, Parkville, Victoria 3052, Australia

[5]Department of Physiology, The University of Melbourne, Parkville, Victoria 3010, Australia

[6]Institute for Molecular Biosciences, The University of Queensland, Brisbane, Queensland 4072, Australia

[7]Peter MacCallum Cancer Centre, Melbourne, Victoria 3000, Australia

[8]Murdoch Children's Research Institute, Parkville, Victoria 3052, Australia

[9]Bioinformatics Division, Walter and Eliza Hall Institute of Medical Research, Parkville, Victoria 3052, Australia

[10]Danish Stem Cell Center, University of Copenhagen, 2200 Copenhagen N, Denmark

[11]Max Planck Institute for Heart and Lung Research, Dept. III – Developmental Genetics

Ludwigstrasse 43, 61231 Bad Nauheim, Germany

[12]Department of Biological Science, National University of Singapore, Singapore

***Corresponding Author:** Joan K Heath, Walter and Eliza Hall Institute of Medical Research, 1G Royal Parade, Parkville, Victoria 3052, Australia. Phone: (+613) 9345-2872

Email: joan.heath@wehi.edu.au

Declaration of interests: The authors declare no potential conflicts of interest

ABSTRACT

The nucleoporin ELYS, encoded by *AHCTF1*, is a large multifunctional protein with essential roles in nuclear pore assembly and mitosis. Using a zebrafish model of hepatocellular carcinoma, in which the expression of an inducible mutant *kras* transgene *($kras^{G12V}$)* drives hepatocyte-specific hyperplasia and liver enlargement, we show that reducing *ahctf1* gene dosage by 50% markedly shrinks tumour burden, while non-hyperplastic tissues are unaffected. We demonstrate that *ahctf1* heterozygosity impairs nuclear pore formation, mitotic spindle assembly and chromosome segregation, leading to DNA damage and activation of TP53-dependent and independent mechanisms of cell death and cell cycle arrest. This selective vulnerability of cancer cells to mild disruption of Elys function uncovers a novel synthetic lethal interaction between *ahctf1* and oncogenic *kras* that could be exploited therapeutically. Heterozygous expression of both *ahctf1* and *ranbp2*, or treatment of heterozygous *ahctf1* larvae with the nucleocytoplasmic transport inhibitor, Selinexor, completely blocked *$kras^{G12V}$*-driven hepatocyte hyperplasia, revealing promising avenues for combinatorial treatments.

INTRODUCTION

Synthetic lethality is the term used to describe the death of cells in response to co-existing disruptions in two different genes, neither of which is lethal alone. The phenomenon has emerged as a promising tool for cancer drug development[1]. The advantage of the approach lies in its capacity to induce the death of a vulnerable cell population, such as oncogene-expressing cancer cells, while healthy cells are unaffected. The approach has been validated in the clinic by the use of poly(adenosine diphosphate [ADP]-ribose) polymerase (PARP) inhibitors to treat tumours carrying mutations in the breast cancer susceptibility genes, *BRCA1*/*BRAC2*[2], and its success has fuelled the search for other clinically relevant pairwise combinations. Particular effort has been directed towards identifying genes whose partial loss of function confers synthetic lethality in cancer cells containing hitherto 'undruggable' oncogene targets, such as mutant *KRAS*[3,4]. In this paradigm, the interacting gene is not mutated in cancer nor oncogenic in its own right; however, its function is essential to maintain the tumourigenic state, inspiring the concept of non-oncogene addiction[5].

In this paper, we tested whether *AHCTF1* exhibits the properties of a mutant *KRAS* synthetic lethal interacting gene. *AHCTF1* encodes ELYS, a 252 kDa multidomain nucleoporin that was first discovered in mouse development where it was shown to be required for the proliferation and survival of inner mass cells[6]. Since then, ELYS has been studied in many model systems, including in a zebrafish development mutant (ti262)[7], where we and others showed that homozygous inheritance of an ENU-induced nonsense mutation in *ahctf1* disrupted nuclear pore formation and caused catastrophic levels of cell death in highly proliferative cell compartments, such as the intestinal epithelium, while relatively quiescent tissues survived and remained healthy[8,9].

That ELYS is selectively required by proliferating cells is not unexpected given the multiple roles it plays in the cell cycle (Fig. 1). As well as being a structural component of nuclear pore complexes (NPCs), ELYS is essential for their formation at the end of mitosis[10-12]. NPCs are huge (110 MDa) multi-subunit complexes comprising at least 30 different nucleoporins (Nups) in an octameric

array[13]. They form cylindrical channels in the nuclear envelope (NE) and regulate nucleocytoplasmic transport and intracellular localisation of large (>40 kDa) molecules. In the absence of ELYS, the NE is re-built at the end of mitosis but this occurs without NPC formation, precluding mRNAs and large proteins from moving in and out of the nucleus. By providing a platform for NPC re-assembly at the end of mitosis (Fig. 1a,b), ELYS restores nucleocytoplasmic trafficking, and thereby facilitates entry into the nucleus of proteins such as G1 and S phase cyclin-dependent kinases that are required for DNA replication and cell cycle progression (Fig. 1c). Also in G1/S phase, ELYS regulates transcription and DNA replication by reversible binding to components of the SWI/SNF 80 chromatin remodeller complex, PBAP, and the DNA replication origin licensing system, MCM2-7, respectively (Fig. 1d-f)[11,12,14,15].

At the end of G2, the cell has grown to a critical size and is prepared for M phase (Fig. 1g). The NE breaks down (NEBD) and NPCs are disassembled (Fig. 1h). Whereas most Nups disperse throughout the cytoplasm and the endoplasmic reticulum (ER)[16,17], ELYS, together with components of the Nup107-160 complex and RANBP2, play an important role in prophase by binding to the kinetochores of recently replicated sister chromatids where they contribute to microtubule recruitment and spindle assembly (Fig. 1i)[18-20]. At telophase, when the chromatids are fully separated, the spindle and kinetochores dissolve and ELYS becomes tethered to thousands of sites on chromatin through its C-terminal chromatin binding region where it promotes chromatin decondensation[15,21]. In G1, the N-terminal half of ELYS provides a scaffold to bind the Nup107-160 complex and other ER-associated Nups, thereby coupling the initiation of NPC assembly with euchromatin formation, restoration of nucleocytoplasmic transport and transcription[11,22,23].

Given this plethora of functions throughout the cell cycle, it is not surprising that ELYS is an Achilles' heel of highly proliferative cells[8,9]. To test whether this vulnerability extrapolates to cancer cells *in vivo*, we employed a highly tractable zebrafish model of hepatocellular carcinoma (HCC) in which hepatocyte hyperplasia and liver enlargement are driven by an inducible, hepatocyte-specific *EGFP-kras*^{G12V} transgene[24]. In this study, we used two-photon microscopy to accurately quantitate liver

volume in the presence and absence of a single nonsense mutation in one allele of the *ahctf1* locus[8,9]. Remarkably, we observed a pronounced reduction in tumour burden in response to this mild (50%) reduction in *ahctf1* gene dosage, while the rest of the animal was unaffected. We further show that this selective vulnerability of oncogenic *kras*^{G12V}-expressing liver cancer cells to *ahctf1* heterozygosity possesses the hallmarks of a synthetic lethal interaction that may be exploited therapeutically.

RESULTS

ahctf1 heterozygosity reduces tumour burden in a zebrafish *kras*^{G12V}-driven model of hepatocellular carcinoma

In the zebrafish *kras*^{G12V}-driven HCC model, the doxycycline-induced expression of a single *EGFP-kras*^{G12V} transgene (genotype denoted *TO(kras*^{G12V}*)*$^{T/+}$ between 2-7 days post-fertilisation (dpf) leads to the accumulation of a constitutively active, EGFP-tagged oncogenic form of Kras specifically in hepatocytes[24] (Fig. 2a). This forced expression of *EGFP-kras*^{G12V} causes hepatocyte hyperplasia and a substantial increase in liver volume that can be quantified by two-photon microscopy. To investigate the role of Elys in a cancer setting, we introduced a mutant *ahctf1* allele (containing a nonsense mutation at codon 1319) from a zebrafish development mutant (*flo*^{ti262})[7] into the genome of this model. This resulted in a 57% reduction in *ahctf1* mRNA expression in *ahctf1*$^{+/-}$ larvae at 7 dpf (Fig. 2b), indicating that the premature codon encoded by the nonsense mutation triggers nonsense mediated decay rather than expression of a truncated Elys protein.

To determine the effect of *ahctf1* heterozygosity (and other treatments) on normal liver cells, we used a control transgenic line, denoted *2-CLiP* (2-Colour Liver Pancreas), in which hepatocytes express dsRed fluorescence but no oncogenic transgene[25]. We found that the mean liver volume in 7 dpf wildtype zebrafish larvae is 1.95 x 10^6 ± 4.99 x 10^4 μm^3 (Fig. 2c,d). *ahctf1* heterozygosity had no significant impact on liver volume in this model, consistent with previous observations that *ahctf1* heterozygotes develop normally, reach sexual maturity, and exhibit a normal lifespan[9].

Turning to the *TO(kras*^{G12V}*)* model, we found that induced expression of oncogenic Kras^{G12V} led to liver hyperplasia and a striking (4.1-fold) increase in liver volume to 7.97 x 10^6 ± 1.21 x 10^5 μm^3. This amounted to an increment in liver volume of approximately 6.02 x 10^6 μm^3 over the course of 5 d, demonstrating the potency of the oncogenic *kras*^{G12V} signal. Remarkably, the excess liver volume was reduced by 35% in livers of *ahctf1*$^{+/-}$;*TO(kras*^{G12V}*)*$^{T/+}$ larvae (down to 5.92 x 10^6 ± 8.83 x 10^4 μm^3). These data demonstrate that a mild (50%) reduction in *ahctf1* gene dosage is sufficient to restrict

tumour burden in livers expressing oncogenic *kras*^{G12V}, while having no effect on normal livers. These results demonstrate that reduced *ahctf1* expression is a selective vulnerability of cancer cells and identify a novel synthetic lethal interaction between *ahctf1* and *kras*^{G12V}.

Robust and persistent overexpression of RAS oncoproteins is frequently associated with oncogene-induced stress comprising defects in DNA replication, DNA damage and genome instability. In the presence of wildtype TP53, this damage is limited by activation of TP53 transcription pathways that induce cell cycle arrest, senescence and apoptosis. To determine whether expression of *kras*^{G12V} causes oncogene-induced stress and Tp53 activation in our model, we measured the levels of Tp53 protein in pooled lysates of micro-dissected *TO(kras*^{G12V}*)*$^{+/+}$ and *TO(kras*^{G12V}*)*$^{T/+}$ livers and the remains of the larvae (Fig. 2e,f). No Tp53 signal was obtained from non-*kras*^{G12V}-expressing livers or the body remains after liver removal. We detected a weak Tp53 signal in extracts of *ahctf1*$^{+/+}$*;TO(kras*^{G12V}*)*$^{T/+}$ livers, indicating that expression of the *kras*^{G12V} oncogene alone elicited a weak Tp53 response. In contrast, a much stronger Tp53 signal (>3.5-fold) was detected in *ahctf1*$^{+/-}$*;TO(kras*^{G12V}*)*$^{T/+}$ livers, demonstrating a more severe level of stress in *ahctf1*$^{+/-}$ hepatocytes expressing oncogenic *kras*^{G12V} than occurs in *ahctf1*$^{+/+}$ hepatocytes.

Loss of Tp53 function enhances *kras*^{G12V}-driven liver enlargement, which is partially alleviated by *ahctf1* heterozygosity

To test whether activation of the Tp53 pathway was involved in reducing the volume of *kras*^{G12V}-expressing livers on a heterozygous *ahctf1* background, we repeated the experiment in the absence of Tp53 function. Here, we utilised the zebrafish *tp53*^{e7} or *tp53*^{M214K} allele, which affects a conserved amino acid residue within a region of the Tp53 DNA-binding domain corresponding to a mutational hotspot in human cancer, producing a transactivation-dead Tp53 variant[26]. Abrogating Tp53 function by homozygous expression of this allele (which we denoted *tp53*$^{m/m}$) in *ahctf1*$^{+/+}$*;TO(kras*^{G12V}*)*$^{T/+}$ larvae supported a further large increase (82%) in excess liver volume ($1.25 \times 10^7 \pm 1.10 \times 10^5$ μm^3) compared to livers on the *tp53*$^{+/+}$ background (Fig. 2g,h) (Supplementary Fig. 1-3). These data

indicate that Tp53 function normally restrains tumour growth and liver enlargement in this model. Nonetheless, the excess liver volume ($9.82 \times 10^6 \pm 1.34 \times 10^5$ μm^3) on the *ahctf1*$^{+/-}$;*tp53*$^{m/m}$;*TO(kras*^{G12V}*)*$^{T/+}$ background was 35% less than on a wildtype *ahctf1* background, indicating that mildly disrupted *ahctf1* expression can reduce tumour burden, even in the complete absence of functional Tp53.

ahctf1 heterozygosity triggers cell death in _TO(kras^{G12V})$^{T/+}$_ hepatocytes that is partially Tp53-independent

As expression of Tp53 was upregulated in *ahctf1*$^{+/-}$;*TO(kras*^{G12V}*)*$^{T/+}$ livers, we next determined whether the reduction in liver volume in heterozygous *ahctf1* larvae was due to the induction of a Tp53-dependent cell death response. To investigate this, we utilised a transgenic line, Tg(*actb2:SEC-Hsa.ANXA5-mKate2,cryaa:mCherry*)^{uq24rp} (hereafter denoted *Annexin 5-mKate*) that constitutively expresses a fusion protein comprising Annexin 5 and the far-red fluorophore mKate[27]. This fusion protein identifies cells undergoing apoptosis by binding to phosphatidylserine that is normally inaccessible on the inner leaflet of the plasma membrane but is exposed as the membrane breaks down. This gives rise to discrete fluorescent puncta, which we captured using confocal imaging.

Annexin 5 fluorescent puncta were sparsely distributed (1.5 puncta per 10^{-5} μm^3) throughout the livers of *ahctf1*$^{+/+}$;*tp53*$^{+/+}$;*TO(kras*^{G12V}*)*$^{T/+}$ larvae demonstrating that expression of *kras*^{G12V} is associated with low levels of cell death (Fig. 3a,b). In marked contrast, the number of Annexin 5 fluorescent objects was 3.5-fold higher (5.2 puncta per 10^{-5} μm^3) in the livers of *ahctf1*$^{+/-}$;*tp53*$^{+/+}$;*TO(kras*^{G12V}*)*$^{T/+}$ larvae demonstrating that the reduction in tumour burden observed in response to *ahctf1* heterozygosity is due, at least in part, to an increase in cell death (Fig. 3a,b left two columns). These results were recapitulated when the cleaved, (active form) of caspase 3 was used as an alternative marker of apoptosis (Supplementary Fig. 4). That cell death in hyperplastic hepatocytes is largely dependent on Tp53 function was demonstrated by negligible apoptosis in the livers of *ahctf1*$^{+/+}$;*tp53*$^{m/m}$;*TO(kras*^{G12V}*)*$^{T/+}$ larvae (Fig. 3a,b right two columns). Again, the effect of

Tp53 loss was partially alleviated by *ahctf1* heterozygosity. We observed a 17.6-fold increase in the abundance of Annexin 5 fluorescent puncta in $tp53^{m/m};TO(kras^{G12V})^{T/+}$ livers on a heterozygous $ahctf1^{+/-}$background, compared to livers on a $ahctf1^{+/+}$ background.

We showed that the elevated level of Tp53 protein observed in $ahctf1^{+/-};TO(kras^{G12V})^{T/+}$ livers, compared to $ahctf1^{+/+};TO(kras^{G12V})^{T/+}$ livers (Fig. 2e,f), was transcriptionally active by the upregulated (4.7-fold) mRNA expression of a canonical Tp53 target gene, *mdm2* (Fig. 3c). This prompted us to quantify the mRNA expression levels of a suite of Bcl2 family genes that regulate intrinsic (mitochondrial) apoptosis (Fig. 3c). Direct Tp53 transcriptional targets, *pmaip1* (aka *noxa*) and *bbc3* (aka *puma*), were both upregulated by >6.5-fold in $ahctf1^{+/-};tp53^{+/+};TO(kras^{G12V})^{T/+}$ livers compared to $ahctf1^{+/+};tp53^{+/+};TO(kras^{G12V})^{T/+}$ livers. mRNAs encoding the other BH3-only apoptosis effector proteins, Bim, Bid, Bik and Bad, and the pro-apoptotic executioner protein, Bax were also increased in $ahctf1^{+/-};tp53^{+/+};TO(kras^{G12V})^{T/+}$ livers compared to $ahctf1^{+/+};tp53^{+/+};TO(kras^{G12V})^{T/+}$ livers. Meanwhile, transcripts encoding Bcl2 and Bclxl pro-survival proteins were significantly downregulated by *ahctf1* heterozygosity. In the absence of Tp53 function, *ahctf1* heterozygosity still increased the expression of these pro-apoptotic transcripts, albeit less markedly. All these data are consistent with induction of Tp53 target genes playing a major role in the cell death response to *ahctf1* heterozygosity in $kras^{G12V}$-expressing livers. Notwithstanding this, *ahctf1* heterozygosity still promotes moderate levels of cell death concomitant with reduced tumour burden, even in the complete absence of Tp53 function.

ahctf1 heterozygosity restricts DNA replication in $TO(kras^{G12V})^{T/+}$ hepatocytes

To explore whether the reduction in liver enlargement we observe in $ahctf1^{+/-};TO(kras^{G12V})^{T/+}$ larvae also involves impaired cell cycle progression, we used an EdU incorporation assay to identify cells in S phase (Fig. 4a). We observed 32% EdU-positive cells in the enlarged livers of $ahctf1^{+/+};tp53^{+/+};TO(kras^{G12V})^{T/+}$ larvae and >20% EdU-positive cells (32% reduction) in the livers of $ahctf1^{+/-};tp53^{+/+};TO(kras^{G12V})^{T/+}$ larvae (Fig. 4b,c). In Tp53 deficient larvae, liver volume was markedly

increased as expected (Fig. 4b) and there was a doubling in the percentage of EdU-positive cells (63% compared to 32%) (Fig. 4c). *ahctf1* heterozygosity reduced liver volume in both Tp53 proficient and deficient larvae (Fig. 4b), consistent with Fig. 2, and reduced the percentage of EdU-positive cells in both Tp53 proficient (22% compared to 32%) and Tp53 deficient larvae (53% compared to 63%) (Fig. 4c). These data indicate that the overall reduction in liver tumour burden we observe in response to *ahctf1* heterozygosity is due to reduced numbers of cycling cells and increased numbers of apoptotic cells.

To investigate this further, we performed RT-qPCR analysis of the negative cell cycle regulators, *cdkn1a* and *cdkn2a/b* in the presence and absence of Tp53. We found that *cdkn1a* and *cdkn2a/*b, encoding p21 and p16, respectively, were upregulated in *ahctf1*$^{+/-}$;*tp53*$^{+/+}$;*TO(kras*^{G12V}*)*$^{T/+}$ livers compared to *ahctf1*$^{+/+}$;*tp53*$^{+/+}$;*TO(kras*^{G12V}*)*$^{T/+}$ livers (Fig. 4d). For *cdkn1a*, this response to *ahctf1* heterozygosity was partially dependent on intact Tp53 function. However, while the level of *cdkn2a/b* mRNA expression was increased in response to *ahctf1* heterozygosity in *tp53*$^{+/+}$;*TO(kras*^{G12V}*)*$^{T/+}$ livers, in this case there was no response to *ahctf1* heterozygosity in *tp53*$^{m/m}$;*TO(kras*^{G12V}*)*$^{T/+}$ livers. This is consistent with *cdkn2a/b* expression being regulated solely by Tp53. To understand the basis for the beneficial effects on tumour burden by *ahctf1* heterozygosity in the absence of Tp53, we investigated the impact of *ahctf1* heterozygosity on the expression of *tp53* family members, *tp63* and *tp73*. We found that *tp63* and *tp73* mRNA expression was up-regulated by 3.0-fold and 2.3-fold, respectively in *ahctf1*$^{+/-}$;*tp53*$^{+/+}$;*TO(kras*^{G12V}*)*$^{T/+}$ livers, compared to *ahctf1*$^{+/+}$;*tp53*$^{+/+}$;*TO(kras*^{G12V}*)*$^{T/+}$ livers. Interestingly, the expression of *tp63* and *tp73* was upregulated by almost the same amount in *ahctf1*$^{+/+}$;*tp53*$^{m/m}$;*TO(kras*^{G12V}*)*$^{T/+}$ livers and this was further enhanced by *ahctf1* heterozygosity (Fig. 4e). These data suggest that in response to *ahctf1* heterozygosity, Tp63 and Tp73, like Tp53, may be capable of promoting *cdkn1a* expression to induce cell cycle arrest even in the absence of functional Tp53. Taken together, the data shown in Figs. 3 and 4 show that *ahctf1* heterozygosity constrains *kras*^{G12V}-driven hepatocyte hyperplasia and liver enlargement by a

mechanism that results in activation of Tp53 family proteins and initiation of transcriptional programs that induce cell cycle arrest and cell death.

ahctf1 heterozygosity disrupts the abundance of nuclear pore complexes in _TO(kras^{G12V})$^{T/+}$_ hepatocytes.

To determine how *ahctf1* heterozygosity leads to Tp53 activation, we examined the integrity of some of the essential processes in which the Elys protein plays a role. As depicted in Fig. 1, Elys fulfils many distinct functions during the cell cycle. Starting with post-mitotic nuclear pore assembly (Fig. 1a), we used confocal laser-scanning microscopy with Airyscan to look at the abundance and distribution of NPCs in thick sections of liver (200 μm) stained with an antibody (mAb414) that recognises FG-repeat Nups (Nup358, 214, 153 and 62) in mature NPCs. Non-*kras^{G12V}* expressing hepatocytes exhibited fluorescent puncta corresponding to NPCs at the nuclear rim with negligible staining in the cytoplasm, a pattern that was unaffected by *ahctf1* genotype (Fig. 5a; left two columns). Upon induction of expression of the *TO(kras^{G12V})$^{T/+}$* transgene, fluorescence intensity was markedly increased in the presence of wildtype *ahctf1* (Fig 5a, third column) and there was an increase in the ratio of nuclear:cytoplasmic staining (Fig 5b). This pattern was different in hepatocytes on a heterozygous *ahctf1* background. Notably, fluorescence intensity at the nuclear rim was partially diminished and this was concomitant with the appearance of puncta in the cytoplasm (Fig. 5a, fourth column; arrows). This apparent reduction in proper NPC assembly resulted in a 21% reduction in the ratio of nuclear:cytoplasmic fluorescence intensity in liver sections (Fig. 5b).

To determine the abundance of NPCs, we analysed images acquired at the nuclear surface (Fig. 5c). The pattern and density of fluorescent puncta observed at the nuclear surface of non-*kras^{G12V}* expressing hepatocytes was not affected by *ahctf1* genotype (Fig. 5c; left two columns). We found 59% more fluorescent puncta/NPCs at the nuclear surface of hyperplastic hepatocytes expressing *kras^{G12V}* in the presence of wildtype *ahctf1*. This *kras^{G12V}*-driven increase in NPCs was reduced by 20%

in response to *ahctf1* heterozygosity (Fig. 5c, d; right two columns). We also observed that induced *kras^{G12V}* expression produced a 28% increase in nuclear volume compared to non-*kras^{G12V}* expressing cells (Fig. 5e), which was reduced to a 13% increase in the context of *ahctf1* heterozygosity. Together, these data indicate that hyperplastic hepatocytes expressing the *kras^{G12V}* oncogene contain more abundant nuclear pores and larger nuclei than their non-*kras^{G12V}* expressing counterparts. While these properties will facilitate nucleocytoplasmic trafficking and be of great benefit towards meeting the transcriptional and translational needs of rapidly cycling cancerous cells, we found that they could not be fully sustained on a *ahctf1$^{+/-}$* background.

ahctf1 heterozygosity impairs mitotic spindle assembly and chromosome segregation in *TO(kras^{G12V})$^{T/+}$* hepatocytes

Next, we examined the impact of reduced Elys expression on spindle formation and chromosome segregation (Fig. 1b). We assessed these features in cryosections of liver using α-tubulin and DAPI to stain microtubules and chromatin, respectively. Metaphase cells in *ahctf1$^{+/+}$;TO(kras^{G12V})$^{T/+}$* livers exhibited normal bipolar spindle formation followed by complete chromosome segregation during anaphase (Fig. 6a). In contrast, metaphase cells in *ahctf1$^{+/-}$;TO(kras^{G12V})$^{T/+}$* hepatocytes displayed abnormal multipolar spindles and misaligned chromosomes (Fig. 6b). Proper chromosome segregation was disrupted with multiple anaphase bridges formed. While the distribution of cells observed at different mitotic stages was similar in *ahctf1$^{+/+}$* and *ahctf1$^{+/-}$* hepatocytes (Fig. 6c), mitotic abnormalities were observed in 50% of *ahctf1$^{+/-}$;TO(kras^{G12V})$^{T/+}$* hepatocytes during metaphase and anaphase but not at all in *ahctf1$^{+/+}$;TO(kras^{G12V})$^{T/+}$* hepatocytes (Fig. 6d). Taken together, these data suggest that hyperplastic hepatocytes require a full complement of *ahctf1* expression to maintain proper cell division.

ahctf1 heterozygosity causes DNA damage in *TO(kras^{G12V})$^{T/+}$* hepatocytes

So far, our results demonstrate that a 50% decrease in *ahctf1* expression has multiple impacts in *TO(kras^{G12V})$^{T/+}$* hepatocytes, including disrupted NPC assembly, impaired mitotic spindle assembly

and incomplete chromosome segregation, consistent with oncogene-induced stress. As several of these defects can converge to produce DNA damage, we looked for evidence of DNA damage by staining cryosections of liver with DAPI and γ-H2AX to mark DNA double-stranded breaks (Fig. 7a,b). We found that while only 1% of *ahctf1*$^{+/+}$*;TO(kras*^{G12V}*)*$^{T/+}$ hepatocyte nuclei were positive for γ-H2AX (Fig. 7c), 6% of *ahctf1*$^{+/+}$*;TO(kras*^{G12V}*)*$^{T/+}$ hepatocyte nuclei were γ-H2AX-positive. Collectively, these data show that the proper functioning of diverse cellular processes in hyperplastic hepatocytes depends on wildtype levels of *ahctf1* expression. We conclude from this that insufficient Elys protein in rapidly cycling cells produces multiple disruptive events that combine to produce elevated levels of oncogene-induced stress and DNA damage, in so doing providing the stimulus to activate Tp53 and transcriptional programs that trigger cell cycle arrest and apoptosis.

Combinatorial approaches can completely restrict *kras*^{G12V}-driven liver hyperplasia

Having determined that heterozygous *ahctf1* mutation is effective in restricting *kras*^{G12V}-driven hepatocyte hyperplasia and liver enlargement, we investigated the potential of targeting cancer via another nucleoporin, Ranbp2, in our zebrafish model of HCC. RANBP2 (also known as NUP358) is a major component of the cytoplasmic filaments of NPCs, where it functions in numerous transport pathways. Like ELYS, RANBP2 also plays non-canonical roles outside of the NPC, including in mitotic progression and the maintenance of genome integrity[28-30]. In colon cancer cells with an activated BRAF signature, RANBP2 silencing reduces microtubule outgrowth from kinetochores, inducing spindle perturbations and cell death, the frequency of which can be exacerbated by treatment with microtubule inhibitors[31].

We identified our zebrafish *ranbp2* mutant in a transgene assisted ENU-mutagenesis screen for mutations affecting endodermal organ morphogenesis[32] and showed, using whole genome sequencing and homozygosity mapping[33,34], that the underlying mutation was a nonsense mutation in *ranbp2* (Supplementary Fig. 5). Like several other mutants we identified in this screen[8,35,36],

mutant *ranbp2* larvae exhibit morphological deficiencies in proliferative compartments, including the developing intestinal epithelium, craniofacial complex and eye (Supplementary Fig. 5).

We found that *ranbp2* heterozygosity alone or in combination with *ahctf1* heterozygosity did not impact on liver volume in *2-CLiP* larvae (Fig. 8a,b). In *TO(kras^{G12V})$^{T/+}$* larvae, liver volume was increased 3.8-fold, as observed previously, and the excess liver volume was reduced by 38% and 13% by the introduction of a single mutation in *ahctf1* or *ranbp2*, respectively (Fig. 8b). Remarkably, we found a striking synergistic benefit of trans heterozygosity in *ranbp2$^{+/-}$;ahctf1$^{+/-}$;TO(kras^{G12V})$^{T/+}$* larvae, to the extent that liver volume was no longer distinguishable from that of normal *2-CLiP* livers. These results show that cancer cells are highly susceptible to combinatorial targeting of Nup function and that it may be possible to exploit this vulnerability to produce highly beneficial outcomes without impacting negatively on healthy tissues.

To examine this concept in a therapeutic context, we assessed the effect of Selinexor, a selective inhibitor of nuclear export (SINE) in our *kras^{G12V}*-driven liver hyperplasia model. Selinexor is an XPO1 (exportin) inhibitor with FDA approval for the treatment of refractory or relapsed multiple myeloma and diffuse large B-cell lymphoma and is in clinical trials for several other cancers, including HCC[37,38]. While we observed no reduction in liver volume in *2-CLiP* larvae exposed to 0.10-2.00 µM Selinexor from 5 to 7 dpf (Fig. 8c,d) (Supplementary Fig. 6), *ahctf1$^{+/+}$;TO(kras^{G12V})$^{T/+}$* larvae exhibited a dose-dependent reduction in liver volume when exposed to Selinexor. Strikingly, liver volume was reduced even further in the context of *ahctf1* heterozygosity, such that at a 1.00 µM dose of Selinexor, *kras^{G12V}*-driven hepatocyte hyperplasia was completely blocked and liver volume was indistinguishable from that of normal, non-hyperplastic *2-CLiP* larvae (Fig. 8c,d). These results indicate that XPO1 inhibition is an effective suppressor of growth and proliferation in our model of mutant Kras-driven HCC, and that its effect is even more impressive when combined with a mild reduction in the expression of the nucleoporin, Elys.

We next examined whether there was any clinical rationale for developing Nup inhibitors for the purpose of cancer treatment. We analysed the survival data of HCC patients (Fig. 8e) collated in the cBioPortal for Cancer Genomics[39,40] in the context of Nup gene expression (Supplementary Table 3). Median overall survival of patients with high mRNA expression of components of the NUP107-160 complex, including ELYS is 21.70 months, whereas the survival of patients with low expression of mRNAs encoding NUP107-160 components is markedly extended to 81.73 months. To be confident of the integrity of this striking result, we investigated whether the gene expression values in the TCGA liver hepatocellular carcinoma (LIHC) dataset were subject to batch effects and unwanted variation, noting that the 372 samples in the LIHC dataset were profiled across 19 sequencing plates. To do this, we performed ANOVAs to assess the effects of individual sequencing plates on the expression of genes encoding components of the NUP107-160 complex (Supplementary Fig. 7). These analyses revealed that differences in gene expression observed between samples were largely unaffected by unwanted variation between sequencing plates.

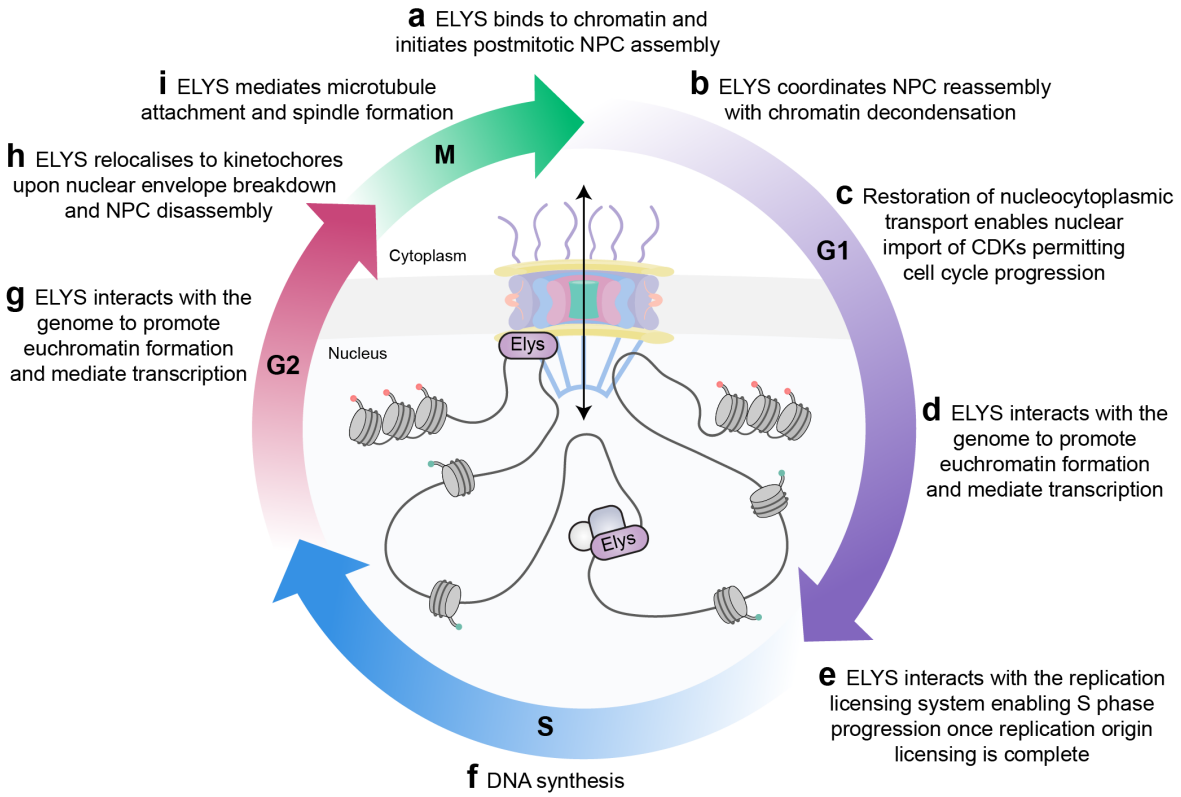

Fig. 1 Elys plays critical roles at several stages of the cell cycle.

Elys is a central player in multiple diverse cellular processes far beyond its canonical role in **a, b.** nuclear pore re-assembly at the end of mitosis. **c.** Elys also restores nucleocytoplasmic trafficking allowing import of cyclin-dependent kinases (CDKs) required for cell cycle progression. **d.** Elys plays an active role in genome regulation through its direct interactions with components of large molecular machineries including chromatin remodellers such as PBAP that favour transcription and **e, f.** the MCM2-7 components of the DNA replication origin licensing system. **g.** After cell growth in G2, **h.** the nuclear envelope breaks down and NPCs are disassembled upon entry into mitosis. Elys relocalises to kinetochores where **i.** it contributes to microtubule attachment and spindle formation.

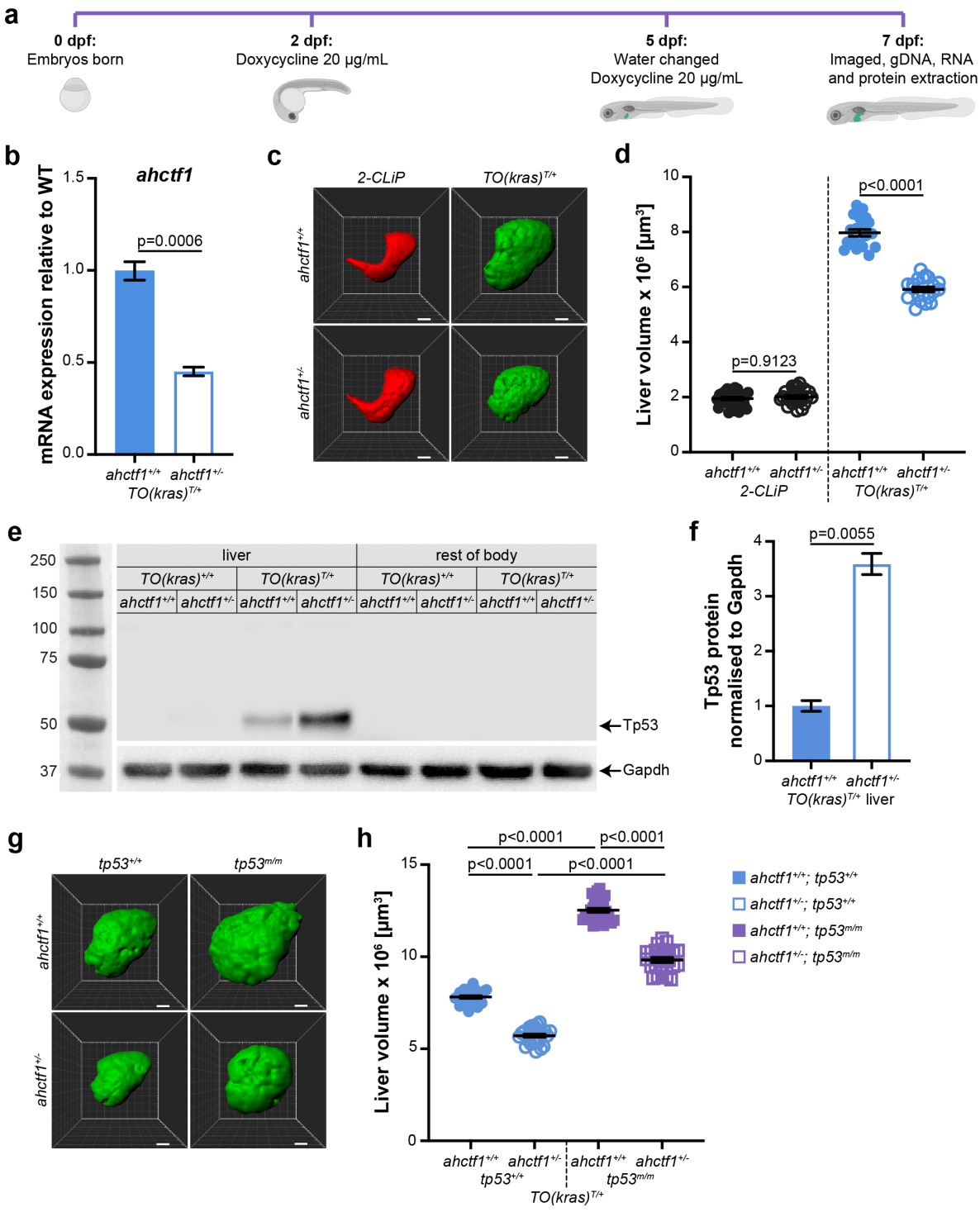

Fig. 2 *ahctf1* heterozygosity reduces liver volume in a zebrafish *kras*^{G12V}-driven model of hepatocellular carcinoma in both Tp53 proficient and deficient larvae.

a. Protocol for doxycycline induction of *TO(kras*^{G12V}*)*$^{T/+}$ expression in developing zebrafish larvae. **b.** RT-qPCR analysis of *ahctf1* mRNA levels in pooled micro-dissected livers (n=3 biological replicates). **c.** Representative three-dimensional reconstructions of *2-CLiP* and *TO(kras*^{G12V}*)*$^{T/+}$ livers of the indicated

358 *ahctf1* genotype. Scale bar 25 µm. **d.** Impact of *ahctf1* heterozygosity on liver volume in *2-CLiP* and
359 *TO(kras^{G12V})$^{T/+}$* larvae (n≥20). **e.** Representative western blot of Tp53 protein signals in lysates of
360 *TO(kras^{G12V})$^{T/+}$* larvae of the indicated *ahctf1* genotype. **f.** Quantification of Tp53 protein levels
361 normalised by reference to the Gapdh loading control (n=3 independent experiments). **g.**
362 Representative three-dimensional reconstructions of *TO(kras^{G12V})$^{T/+}$* livers of the indicated *ahctf1* and
363 *tp53* genotypes. Scale bar 25 µm. **h.** Impact of *ahctf1* heterozygosity and homozygous *tp53* mutation
364 on liver volume in *2-CLiP* and *TO(kras^{G12V})$^{T/+}$* larvae (n≥20). Data are expressed as mean ± SEM.
365 Significance was calculated using a Student's t-test or one-way ANOVA with Tukey's multiple
366 comparisons test.

367

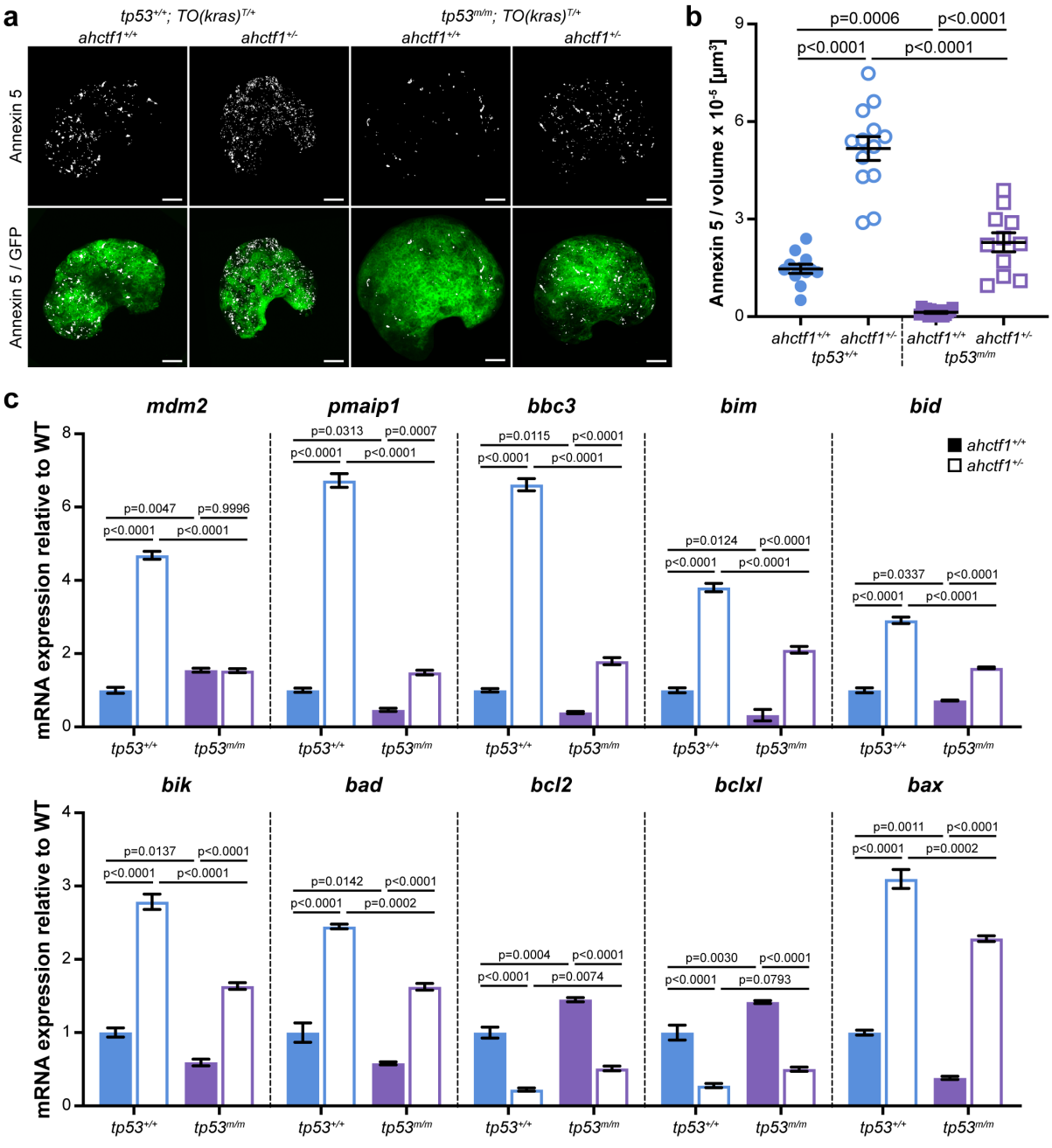

Fig. 3 *ahctf1* heterozygosity increases cell death in *TO(kras^{G12V})$^{T/+}$* hepatocytes in both Tp53 proficient and deficient larvae.

a. Representative maximum intensity projection images of Annexin 5-mKate fluorescence (white puncta), indicating cells undergoing apoptosis in *TO(kras^{G12V})$^{T/+}$* livers of the indicated *ahctf1* and *tp53* genotypes. Scale bar 25 µm. **b.** Quantification of the density of Annexin 5 fluorescent foci in *TO(kras^{G12V})$^{T/+}$* livers of the indicated *ahctf1* and *tp53* genotypes (n≥11). **c.** RT-qPCR analysis of the specified mRNAs in *TO(kras^{G12V})$^{T/+}$* micro-dissected livers of the indicated *ahctf1* and *tp53* genotypes

376 (n=3 biological replicates). Data are expressed as mean ± SEM. Significance was calculated using a

377 one-way ANOVA with Tukey's multiple comparisons test.

378

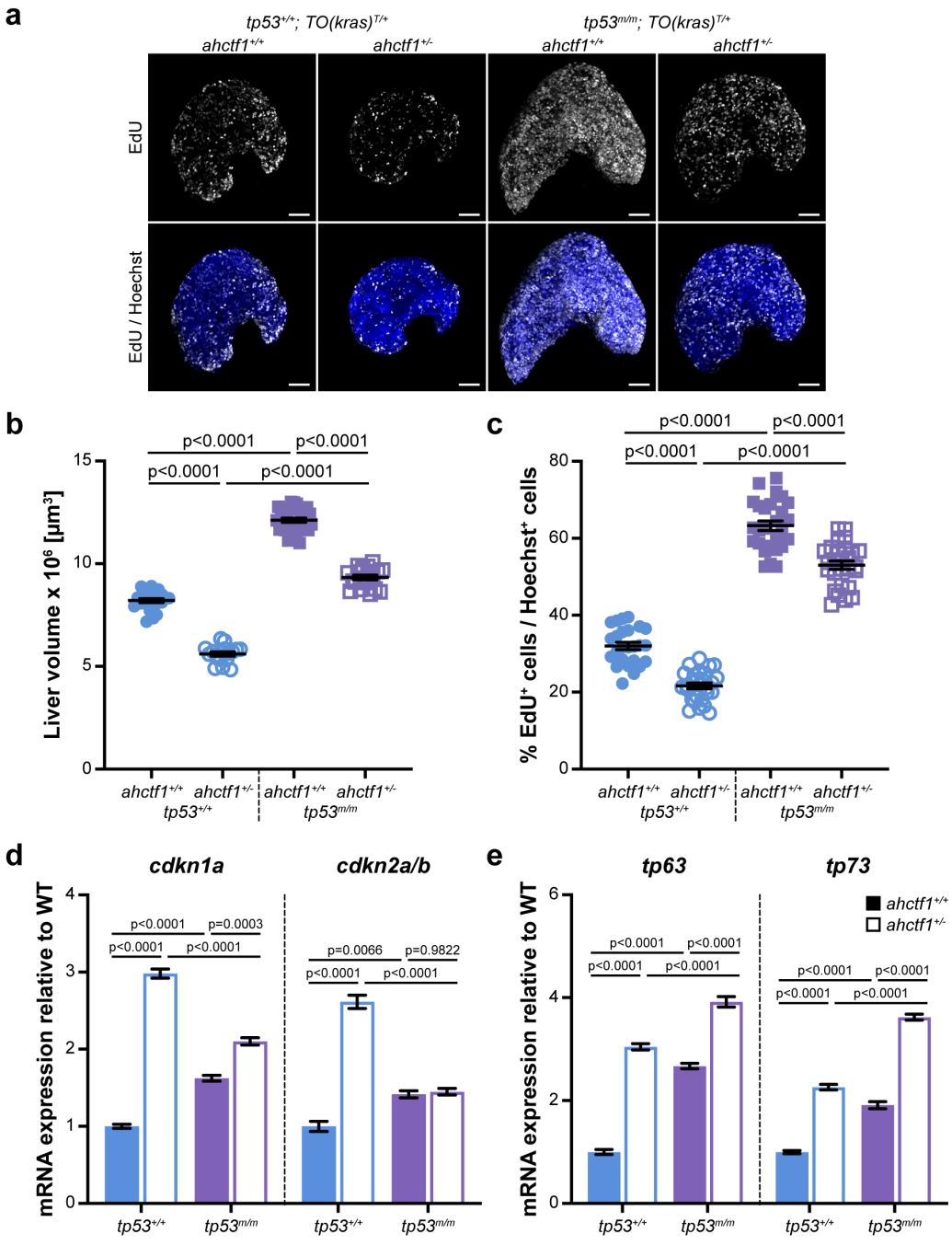

Fig. 4 *ahctf1* heterozygosity restricts DNA replication in *TO(kras^{G12V})$^{T/+}$* hepatocytes.

a. Representative maximum intensity projection images of EdU incorporation (white puncta) into *TO(kras^{G12V})$^{T/+}$* livers of the indicated *ahctf1* and *tp53* genotypes. Scale bar 25 µm. **b.** Impact of *ahctf1* heterozygosity and homozygous *tp53* mutation on liver volume in *2-CLiP* and *TO(kras^{G12V})$^{T/+}$* larvae (n≥17). **c.** Quantification of the percentage of EdU positive nuclei per Hoechst 43332 positive nuclei (n≥25). **d.** RT-qPCR analysis of mRNA expression of the cell cycle regulators, *cdkn1a* and

386 *cdkn2a/b* and **e.** *tp63* and *tp73* in *TO(kras^{G12V})$^{T/+}$* micro-dissected livers of the indicated *ahctf1* and

387 *tp53* genotypes (n=3 biological replicates). Data are expressed as mean ± SEM. Significance was

388 calculated using a one-way ANOVA with Tukey's multiple comparisons test.

389

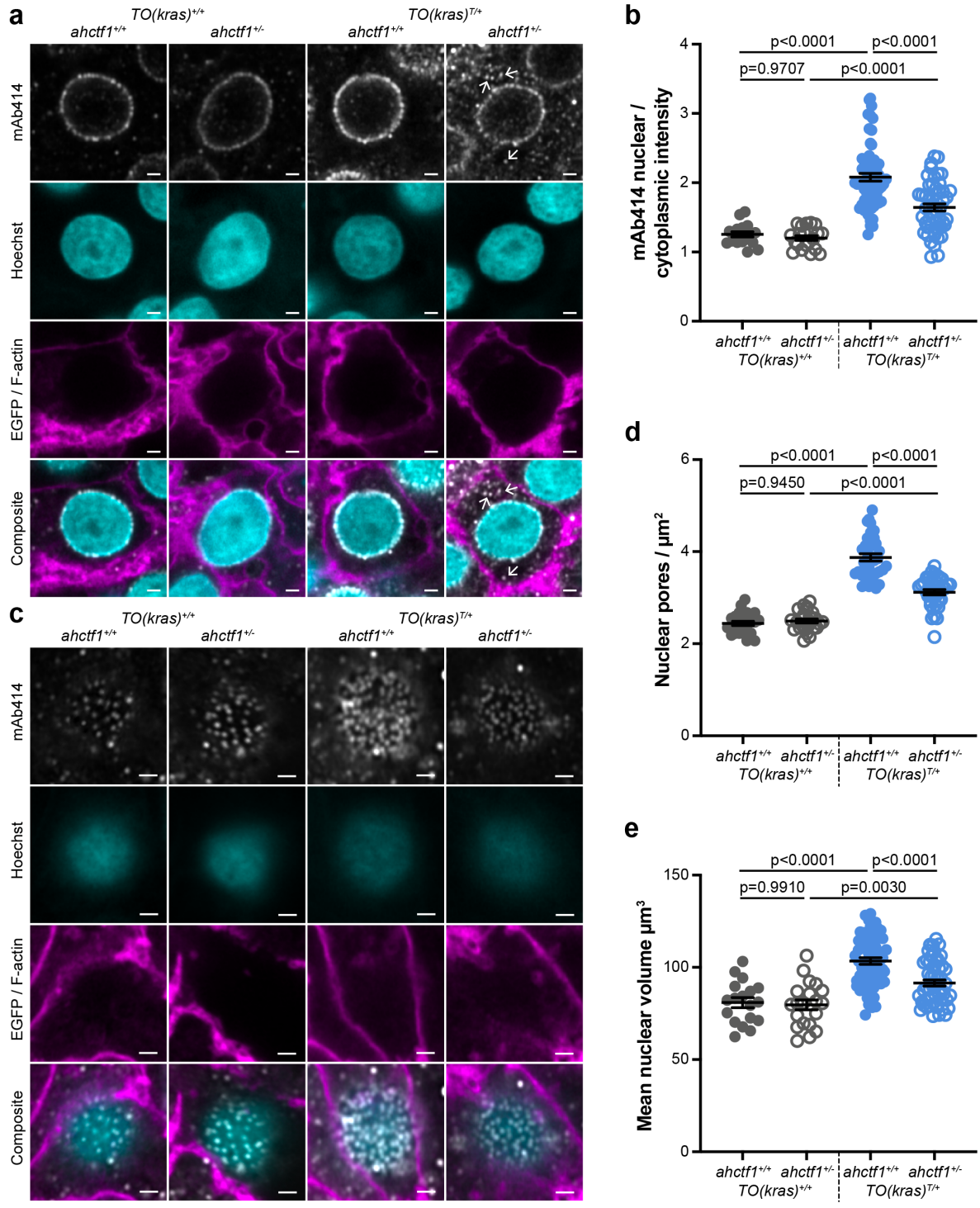

Fig. 5 *ahctf1* heterozygosity disrupts nuclear pore complexes in *TO(kras^{G12V})$^{T/+}$* hepatocytes.

a. Representative Airyscan imaging of liver sections stained with mAb414 (white) marking FG-Nups, Hoechst 43332 (cyan) marking DNA, and rhodamine phalloidin (magenta) marking the F-actin cytoskeleton in non-*TO(kras^{G12V})*-expressing cells or EGFP-Kras^{G12V} (magenta) marking the cell membrane in *TO(kras^{G12V})*-expressing cells of the indicated *ahctf1* and *TO(kras^{G12V})* genotypes.

Arrows indicate mAb414/FG-nucleoporin staining in the cytoplasm. Scale bar 2 µm. **b.** Quantification of mean nuclear/cytoplasmic fluorescence intensity of mAb414 staining after 3D segmentation and morphological filtering of nuclear and cytoplasmic areas (n>18). **c.** Representative Airyscan images of mAb414 staining at the nuclear surface of sections of the indicated *ahctf1* and *TO(kras^{G12V})* genotype. Scale bar 1 µm**. d.** Quantification of nuclear pore density (n≥25). **e.** Quantification of nuclear volume (n≥25). Data are expressed as mean ± SEM. Significance was calculated using a one-way ANOVA with Tukey's multiple comparisons test.

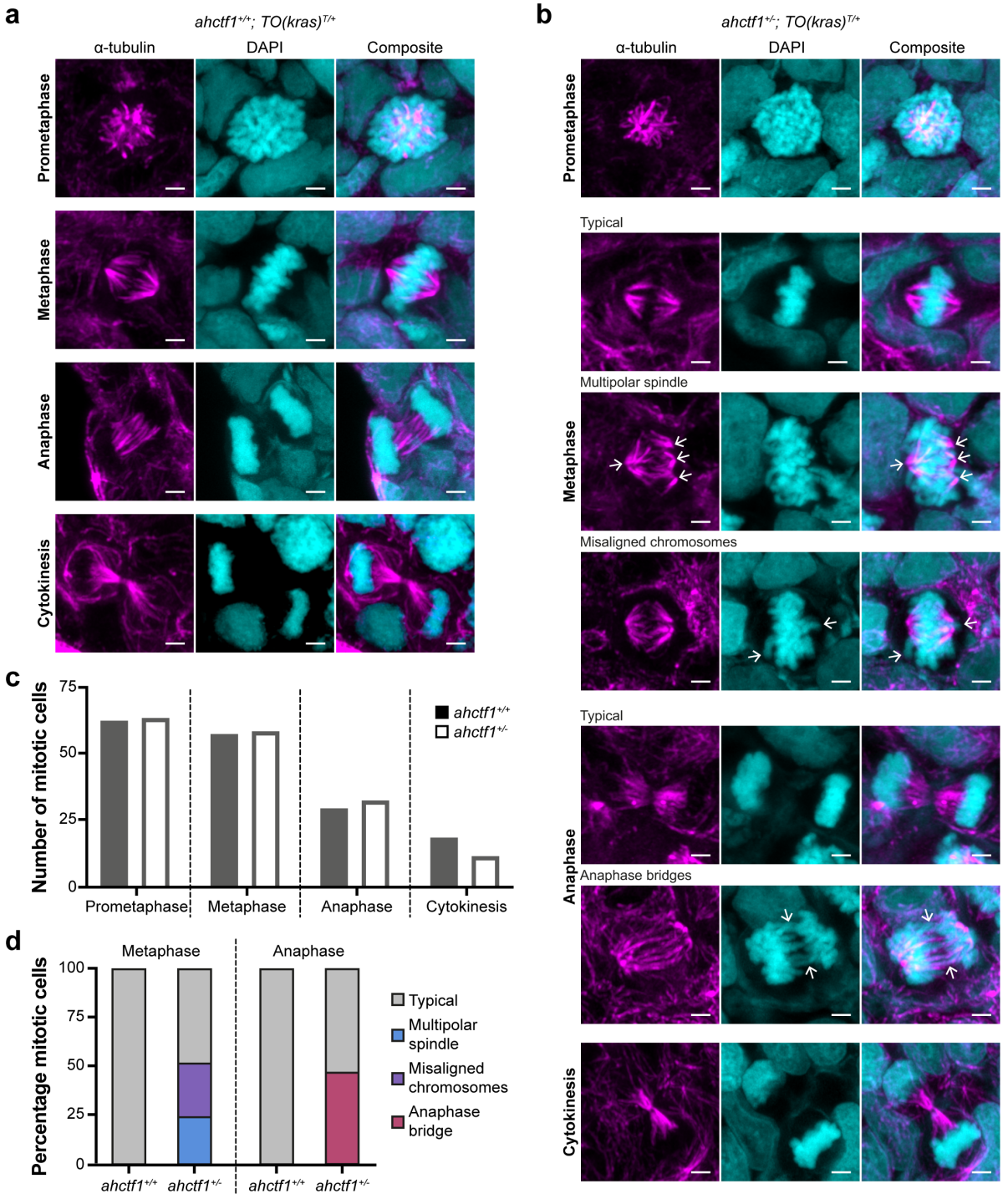

Fig. 6 *ahctf1* heterozygosity impairs mitotic spindle assembly and chromosome segregation in *TO(kras^{G12V})$^{T/+}$* hepatocytes.

a. Representative Airyscan imaging of liver cryosections stained with α-tubulin antibody (magenta) marking spindle microtubules and DAPI (cyan) marking DNA in mitotic cells of *TO(kras^{G12V})$^{T/+}$* larvae on a wildtype *ahctf1$^{+/+}$* background. **b.** Mitotic cells in liver cryosections of *TO(kras^{G12V})$^{T/+}$* larvae on a

410 heterozygous *ahctf1*$^{+/-}$ background exhibit multiple defects, including multipolar spindles, misaligned
411 chromosomes and anaphase bridges (arrows). Scale bar 2 µm. **c.** Distribution of cells observed at
412 different mitotic stages (n=92 livers, 326 mitotic cells) **d.** Quantification of the percentage of mitotic
413 hepatocytes exhibiting an aberrant phenotype (n=14-57).

414

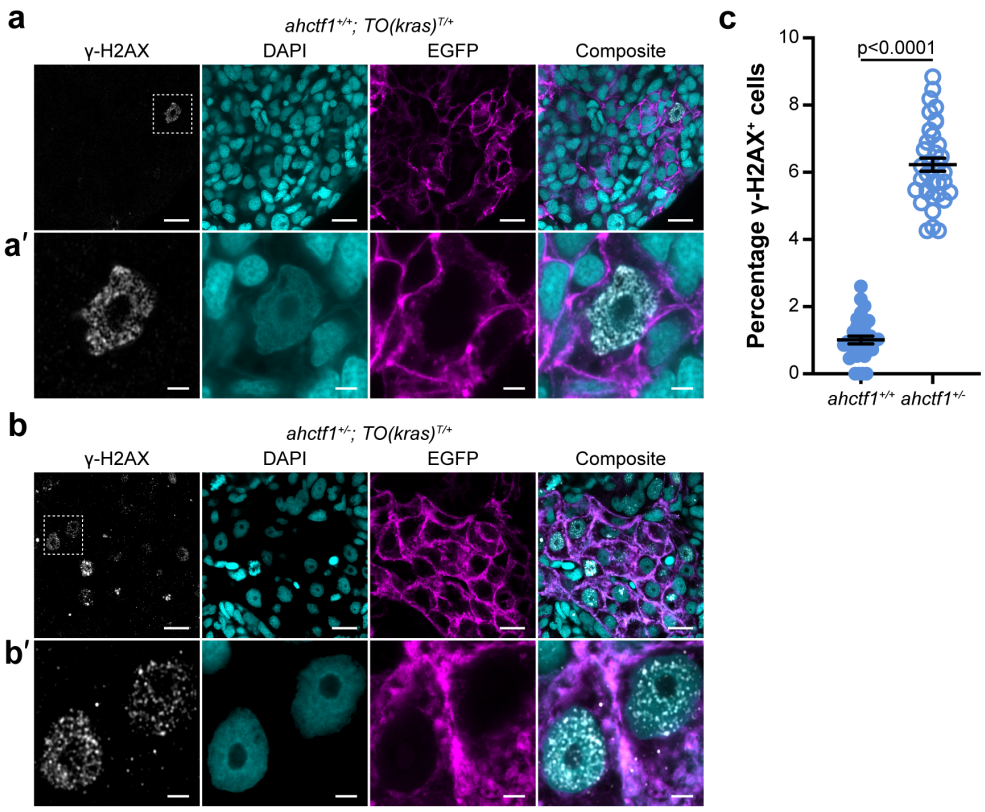

Fig. 7 *ahctf1* heterozygosity leads to accumulation of DNA double-strand breaks in *TO(kras^{G12V})$^{T/+}$* hepatocytes.

a. Representative Airyscan imaging of cryosections of liver from *ahctf1$^{+/+}$;TO(kras^{G12V})$^{T/+}$* larvae stained with γ-H2AX antibody (white) marking DNA double-strand breaks, DAPI (cyan) marking DNA and EGFP-Kras^{G12V} (magenta) marking the cell membrane. Scale bar 5 µm. **a'.** Inset of γ-H2AX positive nuclei in *ahctf1$^{+/+}$;TO(kras^{G12V})$^{T/+}$* hepatocytes. Scale bar 2 µm. **b.** Representative images of cryosections of liver from *ahctf1$^{+/-}$;TO(kras^{G12V})$^{T/+}$* larvae. Scale bar 5 µm. **b'.** Inset of γ-H2AX positive nuclei in cryosections of liver from *ahctf1$^{+/-}$;TO(kras^{G12V})$^{T/+}$* larvae. Scale bar 2 µm. **c.** Quantification of the percentage of hepatocytes positive for γ-H2AX (n≥31). Data are expressed as mean ± SEM. Significance was calculated using a Student's t-test.

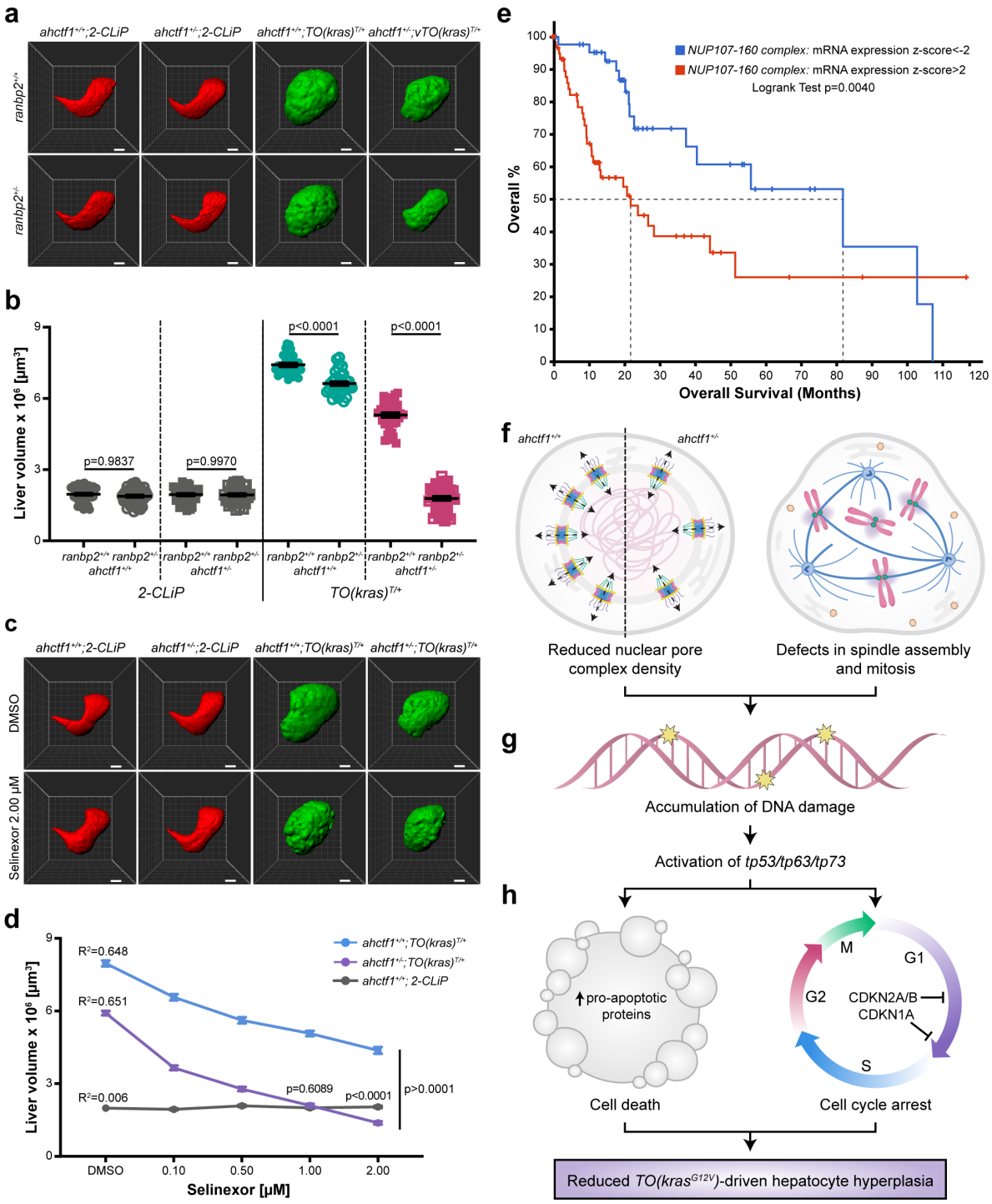

Fig. 8 Combined approaches completely restrict *kras^{G12V}*-driven liver hyperplasia.

a. Representative three-dimensional reconstructions of livers from *2-CLiP* and *TO(kras^{G12V})$^{T/+}$* larvae of the indicated *ahctf1* and *ranbp2* genotypes. Scale bar 25 µm. **b.** Impact of *ahctf1* heterozygosity and *ranbp2* heterozygosity on liver volume in *2-CLiP* and *TO(kras^{G12V})$^{T/+}$* larvae (n≥30). Significance was calculated using a one-way ANOVA with Tukey's multiple comparisons test. **c.** Representative

three-dimensional reconstructions of *TO(kras^{G12V})$^{T/+}$* livers of the indicated *ahctf1* genotype treated with DMSO or 2.00 µM Selinexor from 5-7 dpf. **d.** Dose-dependent impact of Selinexor treatment (0.10-2.00 µM) on liver volume in *2-CLiP* (grey), *ahctf1$^{+/+}$;TO(kras^{G12V})$^{T/+}$* (blue) and *ahctf1$^{+/-}$;TO(kras^{G12V})$^{T/+}$* (purple) larvae (n≥20). Data are expressed as mean ± SEM. Significance was calculated by linear regression analysis. **e.** Overall survival of HCC patients with mRNA expression z-scores >2 for one or more Nup107-160 complex components (red line; 63 cases); median overall survival 21.70 months. Overall survival of HCC patients with mRNA expression z-scores <-2 for one or more Nup107-160 complex components (blue line; 45 cases); median overall survival 81.73 months. Data from the TCGA LIHC dataset (total 372 samples) available in the cBioPortal for Cancer Genomics. **f.** Schematic depiction of two of the processes disrupted by mild depletion of Elys protein culminating in **g.** DNA damage**,** activation of Tp53 transcription programs and **h.** cell death and cell cycle arrest of hyperproliferative Kras^{G12V}-expressing cancer cells.

DISCUSSION

In this paper we show that *ahctf1* heterozygosity markedly reduces tumour burden in a genetically engineered zebrafish model of HCC. In this model of mutant *kras*-driven hepatocyte hyperplasia, *ahctf1* heterozygosity produces a reduction in the density of nuclear pores, aberrant chromatid separation during mitosis (Fig. 8f) and accumulation of DNA damage (Fig. 8g). We propose that these events combine to intensify the oncogene-induced stress sensed by cancer cells induced to hyper-proliferate by expression of the $Kras^{G12V}$ oncoprotein. We also show that the heightened levels of oncogene-induced stress caused by mild depletion of Elys protein provide a powerful stimulus to Tp53 activation. We observed increased abundance of Tp53 protein and enhanced transcription of Tp53 target genes, including *pmaip1* and *bbc3*, encoding two pro-apoptotic BH3-only Bcl2 family proteins (aka Noxa and Puma, respectively), and *cdkn1a* and *cdkn2a/b*, encoding the cell cycle arrest proteins, Cdkn1a/p21 and Cdkn2a/b/p16(Ink4a)/p14(Arf) (Fig 8h). Induced expression of these proteins is typically linked to increased apoptosis and cell cycle arrest. We found no evidence that mild depletion of Elys protein activated this sequence of events in unstressed, non-$kras^{G12V}$-expressing cells.

Our results suggest that the promising therapeutic effect of inhibiting Elys function could be diminished in cancer cells lacking wild-type Tp53 protein. This is a clinically relevant issue since mutations in *TP53*, or amplification/overexpression of its negative regulators *MDM2*/*MDM4*, occur in 30% of HCC cases[41]. To investigate this further, we conducted experiments on a homozygous *tp53* mutant background. We found that *ahctf1* heterozygosity still produced a 24% reduction in tumour burden and induced cell death in the complete absence of Tp53 function, leading us to consider whether the loss of Tp53 function was compensated for by increased *tp63* and/or *tp73* expression. These genes encode Tp53 family proteins that share considerable structural homology with Tp53, particularly within the DNA binding domain, and can activate common and distinct sets of target genes to produce cell cycle arrest, senescence and apoptosis[42,43]. For example, in response to DNA damage, Tp63 induces senescence and apoptosis in the same way as Tp53, via transcriptional

472 induction of *cdkn1a*, *bbc3* and *pmaip1*[44]. We found that *ahctf1* heterozygosity upregulated *tp63* and
473 *tp73* expression by 3.0-fold and 2.3-fold, respectively, and that this was further enhanced by *tp53*
474 mutation. These results suggest a mechanism through which *ahctf1* heterozygosity achieves a
475 reduction in tumour burden in the absence of Tp53 function. Since *TP63* and *TP73* are rarely
476 mutated in cancer[45], it is plausible that inhibition of ELYS function may still produce a beneficial
477 effect on tumour growth in patients harbouring *TP53* mutations.

478 Dysregulation of nucleocytoplasmic transport is a common feature in a broad spectrum of cancers,
479 usually arising from altered expression of nuclear pore components and/or nuclear transport
480 receptors[46]. For example, overexpression of POM121, a transmembrane NPC component, enhances
481 the nuclear import of the pro-proliferation transcription factors, E2F1, MYC and AR, and increases
482 the therapeutic resistance of prostate cancer[47]. Similarly, the nuclear transport receptor XPO1 is
483 frequently overexpressed in cancers, including HCC, and in this case leads to mis-localisation and
484 inactivation of tumour suppressor proteins[38,48]. As a result, numerous selective inhibitors of nuclear
485 export (SINEs) have been developed, including Selinexor (KPT-330), which has advanced through
486 clinical trials and received FDA approval for the treatment of relapsed or refractory multiple
487 myeloma and diffuse large B-cell lymphoma[37]. We found that Selinexor treatment in our zebrafish
488 HCC model produced a dose-dependent reduction in tumour burden. Moreover, this therapeutic
489 effect was strongly augmented by *ahctf1* heterozygosity, suggesting that new drugs targeting the
490 ELYS protein could be combined effectively with drugs that target nucleocytoplasmic transport. We
491 also exploited the genetic tractability of our zebrafish HCC model to show that trans heterozygosity
492 of *ahctf1*, *ranbp2* delivers a synergistic reduction in liver volume/tumour burden, bringing it back to
493 the volume of non-hyperplastic livers. Notably, non-*TO(kras^{G12V})* livers were completely unaffected
494 by *ahctf1*, *ranbp2* trans heterozygosity, indicating a three-pronged synthetic lethal interaction in
495 cancer cells that may be possible to recapitulate with combinatorial drug treatments.

496 There are several reasons why we think our *TO(kras^{G12V})* zebrafish HCC model provides a clinically
497 relevant *in vivo* platform for the study of human cancer and the discovery of new therapeutic

498 strategies[24]. Firstly, RAS/RAF/MAPK signalling is almost always hyper-activated in human HCC[49].
499 Secondly, the progressive accumulation of histopathologic features including irregular nuclei,
500 cytoplasmic vacuolation and increased vascularisation that are characteristic of tumour progression
501 in HCC are reproduced in the zebrafish model[50]. Thirdly, comparative transcriptomic analysis reveals
502 that the gene expression profile exhibited by oncogenic *kras*^{G12V} hepatocytes isolated from larval
503 zebrafish strongly resembles that of early-stage human HCC, with elevated expression of
504 RAS/RAF/MAPK target genes such as *FGFR4, ETV4, EPHA2, DUSP6* and *SPRY* and DNA damage
505 response genes *GADD45B, CCND1* and *H2AX1*[51].

506 Our results compliment a growing body of evidence that carcinogenesis places persistently high
507 demands on essential cellular genes, including those required for proper nuclear pore function,
508 creating a vulnerability that may be therapeutically targeted without causing adverse effects on
509 normal tissue[52,53]. For example, Sakuma *et al*. used siRNAs targeting 28 out of 32 Nup genes, to
510 reduce the abundance of mature NPCs in the human melanoma-derived cell line, A375[52]. Focusing
511 on two Nups exhibiting a severe reduction in NPC density, this study showed that NUP160 and
512 NUP93 are essential for NPC assembly and that inhibiting this process results in cell death.
513 Moreover, they found that cancer cells exhibited heightened susceptibility to inhibition of NPC
514 assembly compared to human pulmonary fibroblasts and a normal cell line derived from retinal
515 pigmental epithelium (RPE1), which instead underwent reversible cell cycle arrest. The differential
516 sensitivity between cancer cells and normal cells to NPC assembly inhibition is consistent with
517 reports that quiescent cells in normal tissues exist for many years with the same set of assembled
518 NPCs and generally maintain low levels of Nup expression[54,55].

519 The dynamic and diverse functions of ELYS require its binding to Nups and many other proteins,
520 including components of kinetochore and replicative licensing complexes, as well as binding to
521 chromatin in various states of condensation. The molecular topology of the ELYS protein and the
522 structural basis for its diverse protein-protein and protein-chromatin interactions are hitherto poorly
523 defined. Crystal structures of ELYS have shown that the β-propeller and α-helical domains in the N-

terminal half of the ELYS protein bind to NUP160, and cryo-electron microscopy reveals the association of the ELYS C-terminal peptide with nucleosomes[21,56]. To advance our molecular understanding of the extent to which discrete domains within the ELYS protein contribute to tumour suppression, further high-resolution structural characterization is required. Hopefully, this will also reveal opportunities to inhibit distinct regions on the protein for the purpose of disabling ELYS function therapeutically. However, even if the topology of ELYS lacked features that would facilitate high affinity binding with small drug-like molecules, as was suggested for other Nups with scaffolding properties[52], rapidly emerging technological advances in drug development are likely to provide alternative strategies to target the ELYS protein. For example, carefully controlled proteasomal degradation of proteins that participate in the oncogenic process with proteolysis targeting chimeras (PROTACs) is a rapidly advancing field in cancer therapy[57]. This approach depends on the availability of a ligand or 'warhead' to direct the PROTAC to the targeted protein, but this need not be a druggable site of protein-protein or protein-chromatin interaction, as is the case for small molecules designed to disrupt the function of the protein. In parallel, emerging small molecule RNA-targeting technology is on course to permit direct modulation of the abundance of specific RNA transcripts for a variety of clinical purposes[58].

In summary, we assert that our *in vivo* cancer studies provide a strong and feasible rationale for targeting ELYS for the treatment of a broad spectrum of cancers. Moreover, our observations with RANBP2, indicate that our findings may be extrapolatable to other multi-functional Nups and provide a foundation for effective combinatorial treatments.

MATERIALS AND METHODS

Zebrafish maintenance and strains

Zebrafish were maintained at 28°C on a 12 h light/12 h dark cycle. The mutant lines *ahctf1*^{ti262} and *tp53*$^{M214K/M214K}$ (also known as *tp53*$^{e7/e7}$ and referred to herein as *tp53*$^{m/m}$) have been described previously[7,26]. Tg(*fabp10:dsRed, ela3l:GFP*)^{gz12}, hereafter referred to as *2-CLiP*, expresses dsRed in the liver and GFP in the exocrine pancreas but carries no oncogenic transgenes or mutations[25]. The Tg(*fabp10:rtTA2s-M2;TRE2:EGFP-kras*^{G12V})^{gz32} line referred to as TO(*kras*^{G12V}) and the cell death reporter line, Tg(*actb2:SEC-Hsa.ANXA5-mKate2,cryaa:mCherry*)^{uq24rp} were described previously[24,27]. The *ranbp2*^{s452} mutant line was generated in the Liver^{plus} ENU mutagenesis screen[32], and its genetic and morphological characterization is presented in this paper.

Inducing hepatocyte hyperplasia in transgenic zebrafish

To induce mutant *kras*^{G12V} expression, *TO(kras*^{G12V}*)* embryos were treated with 20 µg/mL doxycycline (Sigma, #D9891) at 2 dpf in E3 medium (5 mM NaCl, 0.17 mM KCl, 0.33 mM $CaCl_2$, 0.33 mM $MgSO_4$) with 0.003% 1-Phenyl-2-thiourea (PTU; Sigma, #P7629) to suppress pigmentation. E3 medium was changed at 5 dpf and fresh doxycycline (final conc. 20 µg/mL) added. For the Selinexor experiments, the drug (0.10-2.00 mM) (Karyopharm) or 0.001% DMSO (vehicle control) was added at 5 dpf. Morphological and molecular analyses were performed at 7 dpf. To quantitate liver volume, larvae were anaesthetized with benzocaine (200 mg/L) and mounted in 1% agarose. Image acquisition was performed using an Olympus FVMPE- RS multiphoton microscope with a 25x objective and Olympus FV30-SW software. Excitation wavelengths for GFP and RFP were 840 nm and 1100 nm, respectively. For volumetric analysis of whole livers, z-stacks with step-size 2 µm, were imported into ImageJ or Imaris software.

Genotyping

Genomic DNA (gDNA) was extracted from whole zebrafish larvae by incubation at 95°C in 50 µL of 50 mM sodium hydroxide (NaOH) for 20 min, followed by neutralization with 5 µL of 1 M Tris-HCl (pH 8.0). Primer sequences for genotyping are listed in Supplementary Table 1.

mRNA expression analysis

Total RNA was extracted from independent pools of micro-dissected zebrafish livers using the RNeasy Micro Kit (QIAGEN, #74004). RNA integrity was assessed by a High Sensitivity RNA ScreenTape assay (Agilent, #5067-5579) on a 2200 TapeStation. cDNA was generated from 1-10 µg RNA using the Superscript III First Strand Synthesis System (Invitrogen, #18080051) and oligo(dT) priming according to the manufacturer's instructions. RT-quantitative PCR (RT-qPCR) was performed using a SensiMix SYBR kit (Bioline, #QT605-05) on an Applied Biosystems ViiATM7 Real-Time PCR machine. Expression data were normalized by reference to *hrpt1*, *b2m* and *tbp*. LinRegPCR V11.0 was used for baseline correction, PCR efficiency calculation and transcript quantification analysis[59]. Relative expression levels were calculated by the $2^{-\Delta\Delta Ct}$ method and all results were expressed as the mean ± SEM of three independent pools of biological replicates. Primer sequences are listed in Supplementary Table 2.

Western blot analysis

Pooled micro-dissected zebrafish livers were lysed in RIPA buffer (20mM Hepes, pH 7.9, 150mM NaCl, 1mM MgCl2, 1% NP40, 10mM NaF, 0.2mM Na3VO4, 10mM β-glycerol phosphate) supplemented with cOmplete Proteinase Inhibitor (Roche, #11836170001) and PhosTOP phosphatase inhibitors (Roche, #04906837001). Samples were incubated for 30 min on ice and the extracts cleared by centrifugation at 13,000 rpm for 20 min at 4°C. The protein concentration of samples was determined by BCA protein assay (Thermo Fisher Scientific, #23227). 25 µg of protein per lane were resolved on NuPAGE Novex Bis-Tris 4-12% polyacrylamide gels (Invitrogen, #NP0321BOX) and transferred onto nitrocellulose blotting membranes (Amersham Protran,

#10600003). Membranes were blocked with 5% BSA in PBS for 1 h at RT and incubated with primary antibodies 1:500 Anti-p53 (9.1) mouse mAb (Abcam, #ab77813) overnight at 4°C and 1:1000 Anti-GAPDH (14C10) Rabbit mAb (Cell Signalling Technology, #2118) for 1 h at RT. Secondary antibodies: Goat anti-mouse HRP (Dako, #P0447) and Goat anti-Rabbit HRP (Dako, #P0448), were used at 1:5000 and incubated with membranes for 1 h at RT. Signals were developed using Amersham ECL Western Blotting Detection Kit (Cytiva, # RPN2108) and imaged on a Chemidoc Touch (Biorad). Relative protein quantitation was calculated based on normalized integrated intensity.

Cell death analysis

To assess apoptosis, 7 dpf *TO(kras^{G12V});Annexin 5-mKate* zebrafish larvae were fixed in 4% paraformaldehyde (PFA) overnight at 4°C and livers isolated by micro-dissection. Image acquisition was performed using a Zeiss LSM 880 microscope with a 20x objective and ZEN software. Excitation wavelengths for mKate and GFP were 560 nm and 900 nm, respectively. Liver volume was quantified and 3D segmentation of Annexin 5-mKate signals were performed in ImageJ.

Cell cycle analysis

EdU incorporation was used to assess the percentage of cells in S phase of the cell cycle. Briefly, live zebrafish larvae (7 dpf) were incubated at 28°C in 2 mM EdU (Invitrogen, #C10340) in E3 medium for 2 h followed by a further incubation in fresh E3 medium for 1 h. Larvae were euthanised using benzocaine (1000 mg/L; Sigma, #PHR1158) prior to removal of the liver by micro-dissection. EdU labelling was carried out using the Click-iT Edu Alexa Fluor 647 (AF647) imaging kit (Invitrogen, #C10340), according to the manufacturer's instructions. The livers were co-stained with Hoechst 33342 (Thermofisher, #62249). Image acquisition was performed using an Olympus FVMPE-RS multiphoton microscope with excitation wavelengths of 950 nm for Hoechst 33342 dye and 1160 nm for AF647 (Thermofisher, #A21235). The number of Hoechst 33342 and EdU positive cells was quantified using Arivis Vision4D software.

Nuclear pore analysis

Larvae fixed in 4% PFA overnight at 4°C were embedded in 4% low melting temperature agarose and transverse sections collected at 200 µm intervals using a vibrating microtome (Leica VT 1000S). Sections were blocked with 1% BSA in PBS/0.3% Triton X-100 and incubated with a 1:750 dilution of mAb414 (Abcam, #ab24609) at 4°C overnight. Sections were then incubated with 1:500 anti-mouse AF647 and Hoechst 33342 at room temperature for 1 h. Sections were mounted and imaged using a Zeiss LSM880 Fast Airyscan Confocal microscope with a 63x objective. 3D segmentation of cells was performed in ImageJ using EGFP signal for *TO(kras^{G12V})$^{T/+}$* larvae or F-actin stained with 1:200 rhodamine phalloidin for *TO(kras^{G12V})$^{+/+}$* larvae . An outline was drawn around the nuclear periphery as segmented using Hoechst signal. mAb414 fluorescence intensity was calculated for the nuclear periphery and for the cytoplasm. NPC density was calculated by finding maxima for mAb414 at the nuclear surface of 5 nuclei per liver.

Cryosectioning and immunofluorescence microscopy analysis

Dissected livers were fixed in 4% PFA overnight at 4°C and washed with PBS/0.1% Tween 20 before incubation in 30% sucrose in PBS overnight at 4°C. Livers were aligned in a tissue mould, embedded in OCT and frozen on dry ice. The livers were sectioned at 10 µm intervals using a Thermofisher Scientific Microm HM550 cryostat. Sections were washed with PBS before blocking with 10% FCS in PBS/0.3% Triton X-100. Incubation with primary antibodies was performed at 4°C overnight, while incubation with secondary antibodies was performed at room temperature for 1 h. Antibodies used in this work were: 1:2000 α-Tubulin DM1A (CST, #3873), 1:1000 γ-H2AX (gift of James Amatruda), 1:250 cleaved caspase 3 (CST, #9664), 1:500 anti-rabbit AF647 (Thermofisher scientific, #A31573) and 1:500 anti-mouse AF647 (Thermofisher, #A21235). Prolong Diamond Antifade reagent with DAPI (Thermofisher #P36962) was used for slide mounting. A Zeiss LSM880 Fast Airyscan Confocal microscope with a 63x objective was used for image acquisition and ImageJ for image analysis.

641 **Statistical analysis**

642 Data are expressed as mean ± SEM unless indicated otherwise and the number of biological
643 replicates indicating samples from individual animals/livers, or pools of individual animals/livers for
644 each experiment are stated in the figure legends. P-values were calculated using Student's *t*-tests
645 (two-tailed, followed by Welch's correction) when comparing two groups, and by ANOVA followed
646 by Tukey's post-hoc test when comparing multiple groups. The effect of Selinexor treatment on liver
647 volume was analysed by linear regression, regressing liver volume against Selinexor concentration.
648 All analysis was performed using GraphPad Prism V7.03 (GraphPad software) and p-values ≤ 0.05
649 were considered statistically significant.
650

ACKNOWLEDGEMENTS

The authors thank Tyson Blanch, Cameron Mackey, Elizabeth Grgacic and Bryan Ko (zebrafish husbandry), Ellen Tsui (histology), James Amatruda (rabbit polyclonal antibody to zebrafish γ-H2AX), Brendon Monahan and Leigh Coultas (insightful discussions).

COMPETING INTERESTS

The authors declare no competing financial interests.

ADDITIONAL INFORMATION

FUNDING

This work was funded by an Australian Government Research Training Program Scholarship and a WEHI Bridging Fellowship (to KM), the National Health and Medical Research Council of Australia (Grant 1024878 to JKH), Ludwig Cancer Research, a Victorian State Government Operational Infrastructure Support grant, and the Australian Government NHMRC Independent Research Institute Infrastructure Support Scheme.

AUTHORS' CONTRIBUTIONS

KM, KD, JKH conceived and designed the experiments; KM, KD, KS, BH, CS, GB, RM, ATP, TH, EO, DYRS, ZG, JKH developed the methodology; KM, KD, FG, LW, KS, BH, CS, GB, RM, ATP, JKH acquired and analysed the data; KM, KD and JKH wrote the manuscript; KD, JKH supervised the study; JKH acquired the funding.

DATA AVAILABILITY

The datasets generated and/or analysed during the current study are available in the cBioPortal Cancer Genomics database (http://www.cbioportal.org).

673 **REFERENCES**

674 1 Gao, S. & Lai, L. Synthetic lethality in drug development: the dawn is coming. *Future Med*
675 *Chem* **10**, 2129-2132, doi:10.4155/fmc-2018-0227 (2018).

676 2 Lord, C. J. & Ashworth, A. PARP inhibitors: Synthetic lethality in the clinic. *Science* **355**, 1152-
677 1158, doi:10.1126/science.aam7344 (2017).

678 3 Luo, J. *et al.* A genome-wide RNAi screen identifies multiple synthetic lethal interactions with
679 the Ras oncogene. *Cell* **137**, 835-848, doi:10.1016/j.cell.2009.05.006 (2009).

680 4 Wang, T. *et al.* Gene Essentiality Profiling Reveals Gene Networks and Synthetic Lethal
681 Interactions with Oncogenic Ras. *Cell* **168**, 890-903 e815, doi:10.1016/j.cell.2017.01.013
682 (2017).

683 5 Solimini, N. L., Luo, J. & Elledge, S. J. Non-oncogene addiction and the stress phenotype of
684 cancer cells. *Cell* **130**, 986-988, doi:10.1016/j.cell.2007.09.007 (2007).

685 6 Okita, K. *et al.* Targeted disruption of the mouse ELYS gene results in embryonic death at
686 peri-implantation development. *Genes Cells* **9**, 1083-1091, doi:10.1111/j.1365-
687 2443.2004.00791.x (2004).

688 7 Chen, J. N. *et al.* Mutations affecting the cardiovascular system and other internal organs in
689 zebrafish. *Development* **123**, 293-302 (1996).

690 8 de Jong-Curtain, T. A. *et al.* Abnormal nuclear pore formation triggers apoptosis in the
691 intestinal epithelium of elys-deficient zebrafish. *Gastroenterology* **136**, 902-911,
692 doi:10.1053/j.gastro.2008.11.012 (2009).

693 9 Davuluri, G. *et al.* Mutation of the zebrafish nucleoporin elys sensitizes tissue progenitors to
694 replication stress. *PLoS Genet* **4**, e1000240, doi:10.1371/journal.pgen.1000240 (2008).

695 10 Rasala, B. A., Orjalo, A. V., Shen, Z., Briggs, S. & Forbes, D. J. ELYS is a dual
696 nucleoporin/kinetochore protein required for nuclear pore assembly and proper cell
697 division. *Proceedings of the National Academy of Sciences of the United States of America*
698 **103**, 17801-17806, doi:10.1073/pnas.0608484103 (2006).

11 Gillespie, P. J., Khoudoli, G. A., Stewart, G., Swedlow, J. R. & Blow, J. J. ELYS/MEL-28 chromatin association coordinates nuclear pore complex assembly and replication licensing. *Curr Biol* **17**, 1657-1662, doi:10.1016/j.cub.2007.08.041 (2007).

12 Franz, C. *et al.* MEL-28/ELYS is required for the recruitment of nucleoporins to chromatin and postmitotic nuclear pore complex assembly. *EMBO reports* **8**, 165-172, doi:10.1038/sj.embor.7400889 (2007).

13 Beck, M. & Hurt, E. The nuclear pore complex: understanding its function through structural insight. *Nature reviews. Molecular cell biology* **18**, 73-89, doi:10.1038/nrm.2016.147 (2017).

14 Hodgson, B., Li, A., Tada, S. & Blow, J. J. Geminin becomes activated as an inhibitor of Cdt1/RLF-B following nuclear import. *Curr Biol* **12**, 678-683, doi:10.1016/s0960-9822(02)00778-9 (2002).

15 Kuhn, T. M., Pascual-Garcia, P., Gozalo, A., Little, S. C. & Capelson, M. Chromatin targeting of nuclear pore proteins induces chromatin decondensation. *J Cell Biol* **218**, 2945-2961, doi:10.1083/jcb.201807139 (2019).

16 Guttinger, S., Laurell, E. & Kutay, U. Orchestrating nuclear envelope disassembly and reassembly during mitosis. *Nature reviews. Molecular cell biology* **10**, 178-191, doi:10.1038/nrm2641 (2009).

17 Chatel, G. & Fahrenkrog, B. Nucleoporins: leaving the nuclear pore complex for a successful mitosis. *Cell Signal* **23**, 1555-1562, doi:10.1016/j.cellsig.2011.05.023 (2011).

18 Mishra, R. K., Chakraborty, P., Arnaoutov, A., Fontoura, B. M. & Dasso, M. The Nup107-160 complex and gamma-TuRC regulate microtubule polymerization at kinetochores. *Nat Cell Biol* **12**, 164-169, doi:10.1038/ncb2016 (2010).

19 Orjalo, A. V. *et al.* The Nup107-160 nucleoporin complex is required for correct bipolar spindle assembly. *Mol Biol Cell* **17**, 3806-3818, doi:10.1091/mbc.e05-11-1061 (2006).

20 Yokoyama, H. *et al.* The nucleoporin MEL-28 promotes RanGTP-dependent gamma-tubulin recruitment and microtubule nucleation in mitotic spindle formation. *Nat Commun* **5**, 3270, doi:10.1038/ncomms4270 (2014).

21 Kobayashi, W. *et al.* Structural and biochemical analyses of the nuclear pore complex component ELYS identify residues responsible for nucleosome binding. *Commun Biol* **2**, 163, doi:10.1038/s42003-019-0385-7 (2019).

22 Bilokapic, S. & Schwartz, T. U. Molecular basis for Nup37 and ELY5/ELYS recruitment to the nuclear pore complex. *Proceedings of the National Academy of Sciences of the United States of America* **109**, 15241-15246, doi:10.1073/pnas.1205151109 (2012).

23 Rasala, B. A., Ramos, C., Harel, A. & Forbes, D. J. Capture of AT-rich chromatin by ELYS recruits POM121 and NDC1 to initiate nuclear pore assembly. *Mol Biol Cell* **19**, 3982-3996, doi:10.1091/mbc.E08-01-0012 (2008).

24 Chew, T. W. *et al.* Crosstalk of Ras and Rho: activation of RhoA abates Kras-induced liver tumorigenesis in transgenic zebrafish models. *Oncogene* **33**, 2717-2727, doi:10.1038/onc.2013.240 (2014).

25 Korzh, S. *et al.* Requirement of vasculogenesis and blood circulation in late stages of liver growth in zebrafish. *BMC Dev Biol* **8**, 84, doi:10.1186/1471-213X-8-84 (2008).

26 Berghmans, S. *et al.* tp53 mutant zebrafish develop malignant peripheral nerve sheath tumors. *Proceedings of the National Academy of Sciences of the United States of America* **102**, 407-412, doi:10.1073/pnas.0406252102 (2005).

27 Hall, T. E. *et al.* Cellular rescue in a zebrafish model of congenital muscular dystrophy type 1A. *NPJ Regen Med* **4**, 21, doi:10.1038/s41536-019-0084-5 (2019).

28 Joseph, J., Liu, S. T., Jablonski, S. A., Yen, T. J. & Dasso, M. The RanGAP1-RanBP2 complex is essential for microtubule-kinetochore interactions in vivo. *Curr Biol* **14**, 611-617, doi:10.1016/j.cub.2004.03.031 (2004).

29 Salina, D., Enarson, P., Rattner, J. B. & Burke, B. Nup358 integrates nuclear envelope breakdown with kinetochore assembly. *J Cell Biol* **162**, 991-1001, doi:10.1083/jcb.200304080 (2003).

30 Hashizume, C., Kobayashi, A. & Wong, R. W. Down-modulation of nucleoporin RanBP2/Nup358 impaired chromosomal alignment and induced mitotic catastrophe. *Cell Death Dis* **4**, e854, doi:10.1038/cddis.2013.370 (2013).

31 Vecchione, L. *et al.* A Vulnerability of a Subset of Colon Cancers with Potential Clinical Utility. *Cell* **165**, 317-330, doi:10.1016/j.cell.2016.02.059 (2016).

32 Ober, E. A., Verkade, H., Field, H. A. & Stainier, D. Y. Mesodermal Wnt2b signalling positively regulates liver specification. *Nature* **442**, 688-691, doi:10.1038/nature04888 (2006).

33 Leshchiner, I. *et al.* Mutation mapping and identification by whole-genome sequencing. *Genome Res* **22**, 1541-1548, doi:10.1101/gr.135541.111 (2012).

34 Voz, M. L. *et al.* Fast homozygosity mapping and identification of a zebrafish ENU-induced mutation by whole-genome sequencing. *PLoS One* **7**, e34671, doi:10.1371/journal.pone.0034671 (2012).

35 Boglev, Y. *et al.* Autophagy induction is a Tor- and Tp53-independent cell survival response in a zebrafish model of disrupted ribosome biogenesis. *PLoS Genet* **9**, e1003279, doi:10.1371/journal.pgen.1003279 (2013).

36 Markmiller, S. *et al.* Minor class splicing shapes the zebrafish transcriptome during development. *Proceedings of the National Academy of Sciences of the United States of America* **111**, 3062-3067, doi:10.1073/pnas.1305536111 (2014).

37 Jans, D. A., Martin, A. J. & Wagstaff, K. M. Inhibitors of nuclear transport. *Curr Opin Cell Biol* **58**, 50-60, doi:10.1016/j.ceb.2019.01.001 (2019).

38 Zheng, Y. *et al.* KPT-330 inhibitor of XPO1-mediated nuclear export has anti-proliferative activity in hepatocellular carcinoma. *Cancer Chemother Pharmacol* **74**, 487-495, doi:10.1007/s00280-014-2495-8 (2014).

39 Cerami, E. *et al.* The cBio cancer genomics portal: an open platform for exploring multidimensional cancer genomics data. *Cancer Discov* **2**, 401-404, doi:10.1158/2159-8290.CD-12-0095 (2012).

40 Gao, J. *et al.* Integrative analysis of complex cancer genomics and clinical profiles using the cBioPortal. *Sci Signal* **6**, pl1, doi:10.1126/scisignal.2004088 (2013).

41 Zucman-Rossi, J., Villanueva, A., Nault, J. C. & Llovet, J. M. Genetic Landscape and Biomarkers of Hepatocellular Carcinoma. *Gastroenterology* **149**, 1226-1239 e1224, doi:10.1053/j.gastro.2015.05.061 (2015).

42 Levrero, M. *et al.* The p53/p63/p73 family of transcription factors: overlapping and distinct functions. *J Cell Sci* **113 (Pt 10)**, 1661-1670 (2000).

43 Suh, E. K. *et al.* p63 protects the female germ line during meiotic arrest. *Nature* **444**, 624-628, doi:10.1038/nature05337 (2006).

44 Kerr, J. B. *et al.* DNA damage-induced primordial follicle oocyte apoptosis and loss of fertility require TAp63-mediated induction of Puma and Noxa. *Mol Cell* **48**, 343-352, doi:10.1016/j.molcel.2012.08.017 (2012).

45 Dotsch, V., Bernassola, F., Coutandin, D., Candi, E. & Melino, G. p63 and p73, the ancestors of p53. *Cold Spring Harb Perspect Biol* **2**, a004887, doi:10.1101/cshperspect.a004887 (2010).

46 Kau, T. R., Way, J. C. & Silver, P. A. Nuclear transport and cancer: from mechanism to intervention. *Nat Rev Cancer* **4**, 106-117, doi:10.1038/nrc1274 (2004).

47 Rodriguez-Bravo, V. *et al.* Nuclear Pores Promote Lethal Prostate Cancer by Increasing POM121-Driven E2F1, MYC, and AR Nuclear Import. *Cell* **174**, 1200-1215 e1220, doi:10.1016/j.cell.2018.07.015 (2018).

48 Hill, R., Cautain, B., de Pedro, N. & Link, W. Targeting nucleocytoplasmic transport in cancer therapy. *Oncotarget* **5**, 11-28, doi:10.18632/oncotarget.1457 (2014).

49 Calvisi, D. F. *et al.* Ubiquitous activation of Ras and Jak/Stat pathways in human HCC. *Gastroenterology* **130**, 1117-1128, doi:10.1053/j.gastro.2006.01.006 (2006).

50 Zheng, W. *et al.* Xmrk, kras and myc transgenic zebrafish liver cancer models share molecular signatures with subsets of human hepatocellular carcinoma. *PLoS One* **9**, e91179, doi:10.1371/journal.pone.0091179 (2014).

51 Huo, X. *et al.* Transcriptomic analyses of oncogenic hepatocytes reveal common and different molecular pathways of hepatocarcinogenesis in different developmental stages and genders in kras(G12V) transgenic zebrafish. *Biochem Biophys Res Commun* **510**, 558-564, doi:10.1016/j.bbrc.2019.02.008 (2019).

52 Sakuma, S. *et al.* Inhibition of Nuclear Pore Complex Formation Selectively Induces Cancer Cell Death. *Cancer Discov* **11**, 176-193, doi:10.1158/2159-8290.CD-20-0581 (2021).

53 Beck, M., Schirmacher, P. & Singer, S. Alterations of the nuclear transport system in hepatocellular carcinoma - New basis for therapeutic strategies. *J Hepatol* **67**, 1051-1061, doi:10.1016/j.jhep.2017.06.021 (2017).

54 D'Angelo, M. A., Raices, M., Panowski, S. H. & Hetzer, M. W. Age-dependent deterioration of nuclear pore complexes causes a loss of nuclear integrity in postmitotic cells. *Cell* **136**, 284-295, doi:10.1016/j.cell.2008.11.037 (2009).

55 Toyama, B. H. *et al.* Identification of long-lived proteins reveals exceptional stability of essential cellular structures. *Cell* **154**, 971-982, doi:10.1016/j.cell.2013.07.037 (2013).

56 Bilokapic, S. & Schwartz, T. U. Structural and functional studies of the 252 kDa nucleoporin ELYS reveal distinct roles for its three tethered domains. *Structure* **21**, 572-580, doi:10.1016/j.str.2013.02.006 (2013).

57 Ocana, A. & Pandiella, A. Proteolysis targeting chimeras (PROTACs) in cancer therapy. *J Exp Clin Cancer Res* **39**, 189, doi:10.1186/s13046-020-01672-1 (2020).

58 Mukherjee, H. *et al.* PEARL-seq: A Photoaffinity Platform for the Analysis of Small Molecule-RNA Interactions. *ACS Chem Biol* **15**, 2374-2381, doi:10.1021/acschembio.0c00357 (2020).

59 Ruijter, J. M. *et al.* Amplification efficiency: linking baseline and bias in the analysis of quantitative PCR data. *Nucleic Acids Res* **37**, e45, doi:10.1093/nar/gkp045 (2009).